minerals

MDPI

Article

Mineralogically Constrained Fluid–Solid Coupled Simulation of Fracture Network Initiation and Propagation in Tight Sandstone

Xin Qiu [1,2], Mian Lin [1,2,*], Wenbin Jiang [1,2], Gaohui Cao [1,2], Wenchao Dou [1,2] and Lili Ji [1,2]

[1] Institute of Mechanics, Chinese Academy of Sciences, Beijing 100190, China; qiuxin@imech.ac.cn (X.Q.); jiangwenbin@imech.ac.cn (W.J.)
[2] School of Engineering Science, University of Chinese Academy of Sciences, Beijing 100049, China
* Correspondence: linmian@imech.ac.cn

Abstract

Hydraulic fracture network initiation and propagation in tight sandstone are strongly controlled by mineral heterogeneity and fluid–solid interaction. However, existing numerical models still have limited capability in simultaneously representing multi-mineral distributions and dynamically coupled fracture-fluid processes. In this study, a two-dimensional polygonal discrete element fluid–solid coupled model was established based on mineralogical images of tight sandstone. Compared with conventional continuum-based approaches, the proposed model is better suited to describing fracture initiation, branching, and network evolution in multi-mineral granular media. Under dimensionless operating conditions calibrated against field data, coupled and uncoupled formulations were systematically compared to evaluate the role of hydro-mechanical interaction during hydraulic fracturing. The coupled simulations generated consistently more fractures than the uncoupled simulations over the investigated injection-rate range, with an average increase of 28.7% and a maximum increase of 67.2%. Compared with the uncoupled model, the coupled model also predicted higher breakdown pressures and stronger fracture-tip pressure concentrations, and the breakdown pressure increased with injection rate. Under low injection rates, the coupled formulation reproduced pressure-buildup-driven fracture-tip advance, whereas the uncoupled formulation failed to sustain fracture propagation. Under higher injection rates, the coupled formulation produced multilayered and highly branched fracture networks, while the uncoupled formulation mainly generated simple first-order branching. These results demonstrate that hydro-mechanical coupling is a controlling mechanism for fluid-energy dissipation, fracture-tip pressure evolution, and complex fracture network formation in tight sandstone. This study provides an image-based polygonal DEM framework for evaluating hydro-mechanical fracture network evolution in multi-mineral tight sandstone.

Keywords: tight sandstone; multi-mineral heterogeneity; hydraulic fracturing; fluid–solid coupling; fracture network propagation; polygonal discrete element model

Check for updates

Academic Editor: Cristina Gama

Received: 10 April 2026
Revised: 9 May 2026
Accepted: 15 May 2026
Published: 17 May 2026

Copyright: © 2026 by the authors. Licensee MDPI, Basel, Switzerland. This article is an open access article distributed under the terms and conditions of the Creative Commons Attribution (CC BY) license.

1. Introduction

Improving the recovery efficiency of tight oil and gas has long been a central focus in the engineering community. The creation of large-scale, complex fracture networks through hydraulic fracturing represents an effective strategy for the efficient development of tight oil and gas reservoirs [1]. However, the fundamental factors and mechanical mechanisms

that control the initiation and propagation of fracture networks in tight sandstones remain poorly understood.

The generation and propagation of fracture networks in rocks are fundamentally controlled by the reservoir stress field and the intrinsic properties of the rock [2]. In engineering practice, these factors are typically assessed using macroscopic parameters, such as the rock brittleness index, which is commonly employed to estimate fracture propagation potential. However, such indices fail to fully capture the complexity of fracture growth and network development, particularly in tight sandstones. Therefore, the mineralogical composition and microstructural arrangement of the rock play a pivotal role, necessitating a microscopic examination of inter-grain interactions to accurately understand fracture network evolution. At the grain scale, hydraulic fractures may propagate through mineral grains, deflect along intergranular boundaries, or branch near mechanically weak mineral phases. These processes cannot be fully interpreted using only macroscopic brittleness indices or homogeneous continuum assumptions.

Numerical simulation has become an indispensable tool for investigating the growth mechanisms of fracture networks [3–5]. Recent studies using microscopic rock models have shown that mineral composition and distribution exert a significant influence on fracture network formation across various lithologies, including granite [6], conglomerate [7], tight sandstones [8], and shale [9]. In addition, recent grain-scale hydraulic fracturing models have made important progress in representing polymineralic rock microstructures and fluid-driven cracking. For example, coupled hydro-grain-based discrete element models have been used to investigate fluid-driven microcracking behavior and the influence of grain-scale mechanical parameters on hydraulic fracturing in crystalline rocks [10,11]. Grain-based DEM coupled with pore network models has also been developed to study the interaction between hydraulic fractures and inherent microstructures in polymineralic rocks [12]. Moreover, hydro-grain-based models combined with discrete fracture network descriptions have been applied to investigate hydraulic fracture propagation in rocks containing complex natural fracture networks [13]. These studies demonstrate that mineral-scale or grain-scale heterogeneity is a key factor controlling fracture path selection, fracture asymmetry, and branching behavior.

However, these studies are largely qualitative and generally overlook the interaction between applied fluid pressure and fracture network development [14]. As hydraulic fracturing represents a classic fluid–solid coupled process, numerical models are commonly classified as either coupled or uncoupled to balance physical realism with computational feasibility. The uncoupled approach, characterized by a "fluid-driven solid" framework, treats fluid pressure as an external load applied to the rock, neglecting the feedback from fracture propagation on the fluid field. To facilitate parametric sensitivity analyses, some researchers have simplified fracture morphology to approximate the effects of fluid, such as P3D analytical-numerical methods [15,16] derived from the classical PKN model [17,18] and FEM models with pre-defined fracture growth [19–22]. While these methods exhibit robust convergence and high computational efficiency, they are incapable of capturing the underlying fracture failure mechanisms.

Fluid–solid coupled methods provide bidirectional feedback at temporal or iterative scales, enabling the simulation of complex processes such as fracture branching and network evolution. These approaches can be broadly categorized as follows: (1) Discrete element methods (DEM), which have recently evolved into DEM-CFD or DEM-LBM coupled frameworks. In these models, the solid phase is tracked in a Lagrangian framework via DEM, while the fluid phase is resolved on a Eulerian mesh using the Navier–Stokes equations or the Lattice Boltzmann Method (LBM). Coupling is achieved by synchronously updating the forces exerted by the fluid on particles and the feedback of particle motion on

the fluid field. However, rock representations typically employ geometrically simplified elements, such as triangular [23,24], rectangular [25], and circular [26,27], and lack mineralogical heterogeneity, treating particles as homogeneous solids [28]. Recent Hydro-GBM and GBM-PNM studies have partly addressed this limitation by incorporating grain-scale heterogeneity and fluid flow into rock fracture simulations [10–12]. Nevertheless, these models have been mainly applied to crystalline or polymineralic rocks, and the direct use of BSE-EDS-derived mineral maps for constructing tight sandstone polygonal DEM models remains limited. (2) Continuum-based methods, such as the coupling of Biot's poroelastic theory with XFEM [29,30] or phase-field methods (FPM) [31–33], allow for flow-stress coupling at the continuum scale and can simulate complex fracture growth, branching, and interaction with pre-existing fractures. However, because mineral grains and intergranular boundaries are usually homogenized in continuum formulations, these methods cannot explicitly capture the interactions between hydraulic fractures and mineral-scale microstructures. (3) Hybrid approaches, such as the finite-discrete element method (FDEM) [34], integrate independent block fracture motion from DEM with deformable meshes from FEM, maintaining flow governed by Poiseuille's law and continuity equations, yet at extremely high computational cost. Recent FDEM studies have demonstrated strong capability in simulating coupled thermo-hydro-mechanical fracturing processes and fracture interaction with discontinuities, but their computational cost remains a challenge for systematic microstructure-based parametric studies.

Collectively, the remaining limitation lies in the insufficient integration of real mineral maps, polygonal DEM-based representation of tight sandstone microstructure, efficient fluid–solid coupling, and systematic coupled/uncoupled comparison under dimensionless injection-rate scaling. Such an integrated framework is needed to isolate the role of fluid–solid coupling and to clarify how mineral-scale heterogeneity affects fracture nucleation and propagation in tight sandstone.

To address these challenges, we develop a new fluid–solid coupled model. The spatial distribution of the main mineral groups in tight sandstone was extracted from BSE (Backscattered Electron imaging)—EDS (Energy-Dispersive X-ray Spectroscopy) mineral maps and incorporated into the two-dimensional polygonal discrete-element model following reference [8]. In this model, the major mineral groups were assigned equivalent mechanical and intergranular bonding properties. Fluid flow is solved on the DEM lattice via the cubic law, enhancing computational efficiency. By explicitly coupling fluid elements with mineral particles, we construct a hydraulic-fracturing model that we benchmark against an uncoupled variant, and we investigate how variations in fluid loading govern the nucleation and propagation of fracture networks in tight sandstone.

2. Numerical Model

2.1. Construction of Tight Sandstone Models Based on BSE-EDS Images

The Ordos Basin, located in north-central China, is one of the most important petroliferous basins in China and contains extensive tight sandstone reservoirs [35]. These reservoirs are generally characterized by low porosity, low permeability, and strong mineralogical heterogeneity, making hydraulic fracturing essential for effective reservoir stimulation. Therefore, tight sandstone core samples from the Ordos Basin were selected in this study to construct mineral-based numerical models. The construction workflow of the tight sandstone hydraulic fracturing model based on BSE-EDS images is illustrated in Figure 1. Core samples from the Ordos Basin tight sandstone were first sectioned, and corresponding BSE-EDS images were acquired. Backscattered Electron imaging (BSE) provides grayscale contrast mainly related to the average atomic number of minerals, whereas Energy-Dispersive X-ray Spectroscopy (EDS) provides elemental compositional information. Therefore, the

combined BSE-EDS method can be used to identify and distinguish different mineral phases in the rock sample. The microstructural heterogeneity of tight reservoirs varies significantly [36], necessitating an analysis of a representative field-of-view (FOV) for the sandstone model, as shown in Figure 2. When the FOV reaches 3.5 mm, the variation in the major mineral proportions decreases to less than 0.1%, indicating that the mineral distribution becomes representative. Therefore, a 6 mm BSE-EDS image was selected as the initial mineral distribution for constructing the fracturing model, adequately capturing the micro-scale representative elementary scale (RES) of the tight sandstone reservoir.

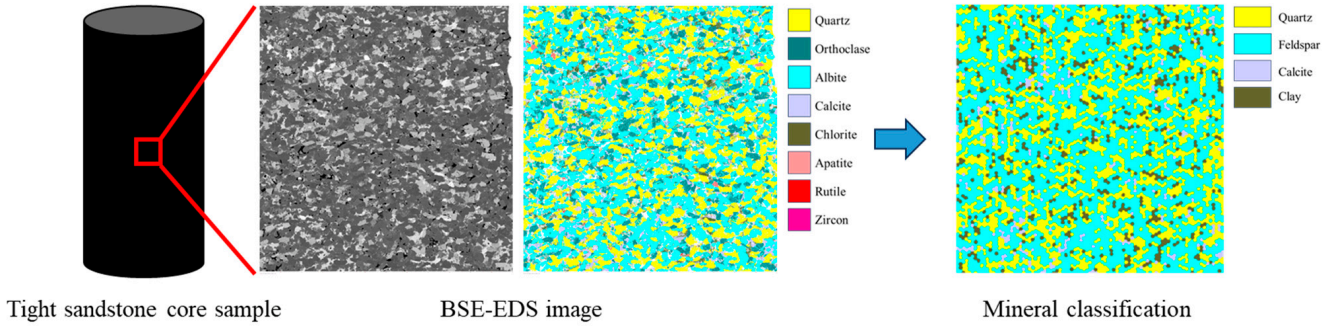


Figure 1. Construction of the tight sandstone hydraulic fracturing model based on BSE-EDS images (mineral colors indicated throughout).

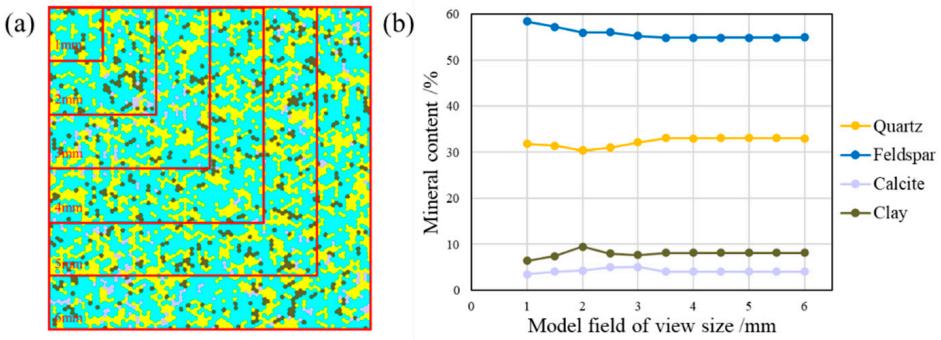


Figure 2. Representative analysis of BSE-EDS images: (**a**) segmentation of the tight sandstone model field of view from 1 to 6 mm; (**b**) statistical variations in mineral content within the segmented fields.

BSE-EDS imaging enables detailed analysis of the mineral composition and spatial distribution within tight sandstones. To simplify the DEM model while retaining the main mineralogical features, the minerals identified from the BSE-EDS images were reclassified into four representative groups. Orthoclase and albite were merged into feldspar; chlorite was assigned to clay minerals; and calcite was assigned to carbonates. Minor accessory minerals, including apatite, rutile, and zircon, as well as pores with very small area fractions, were merged into adjacent or mineralogically/mechanically similar phases according to their local spatial context. Mineralogical analysis indicates that quartz, feldspar, clay minerals, and carbonates together account for over 99% of the rock, allowing the simplification of the mineral composition into these four categories for this study. In this study, clay minerals were treated as an equivalent mineral phase because the main focus was on the mechanical contrast and spatial distribution of major mineral groups. The effects of different clay mineral species were not explicitly considered.

A square model was constructed based on the image dimensions, and discretization was performed. In the discrete element method (DEM), objects are typically represented by circular or polygonal elements. Circular particles, however, hinder the incorporation of interlocking effects characteristic of minerals and generate an excessive number of interparticle pores, which are inconsistent with the physical properties of tight rocks. To better

replicate the physical behavior of tight sandstone, polygonal elements were employed. The classified four-phase mineral map was converted into a DEM model using a pixel-to-particle mapping method. The mineral image was first resampled by nearest-neighbor interpolation, and each pixel was classified as quartz, feldspar, carbonates, or clay minerals according to the minimum weighted color distance in RGB and CIELAB color spaces. A Voronoi polygonal mesh was then generated in the square model domain. For each polygonal particle, the centroid was calculated and mapped to the corresponding position in the mineral label matrix. The mineral label at this position was assigned to the particle, producing a DEM model composed of approximately 6900 polygonal mineral particles. The corresponding mineral-specific mechanical parameters were then assigned for hydraulic fracturing simulation. The model applies in situ stresses along the boundaries, with a central injection point representing fluid introduction.

In discrete element simulations, the micro-scale parameters at interfaces between different mineral particles are primarily determined through micro-mineral testing, rock mechanics experiments, and empirical correlations. In the hydraulic fracturing model, micro-strength and stiffness parameters at interfaces between distinct mineral particles were assigned based on differences in mechanical properties obtained from nanoindentation experiments [37], and using a weighted intergranular boundary parameter approach [38], as summarized in Tables 1 and 2. The normal and tangential stiffness of the boundaries were both set to 0.6.

Table 1. Intra-particle micro-parameters of mineral particles in the tight sandstone fracturing model.

Variable	Value			
	Quartz	**Feldspar**	**Carbonate Mineral**	**Clay Mineral**
Density (ρ, g/cm^3)	2.65	2.71	2.712	2.72
Tensile Strength (σ_n, MPa)	5.8	5.4	5.0	4.5
Cohesion (c, MPa)	15	12	10	8.8
Internal friction angle (θ, °)	30	30	30	30

Notes: In Table 2, "Carbonate mineral" is abbreviated as "Carbonate," and "Clay mineral" is abbreviated as "Clay".

Table 2. Inter-particle micro-parameters of mineral particles in the tight sandstone fracturing model.

Mineral Interfaces			NormalStiffness (k_n, GPa/m)	TensileStrength (σ_n, MPa)
Type	**Mineral 1**	**Mineral 2**		
1	Quartz	Quartz	12.0	1.74
2	Quartz	Feldspar	9.7	1.68
3	Quartz	Clay	6.7	1.55
4	Quartz	Carbonate	10.8	1.62
5	Feldspar	Feldspar	7.4	1.62
6	Feldspar	Clay	4.4	1.49
7	Feldspar	Carbonate	8.5	1.56
8	Clay	Clay	1.3	1.35
9	Clay	Carbonate	5.5	1.43
10	Carbonate	Carbonate	9.6	1.50

2.2. Principles of Fluid–Solid Coupled Computation

The fracturing model is based on 2D KGD theory, with the influence of model thickness in the vertical direction on fracture propagation neglected. In the coupled model, tight sandstone is represented by polygonal particles, whose motion is governed by the equations of motion, while fracturing fluid flow is described by the cubic law. The forces exerted

by the fluid are applied to the particles as external loads, and the particle motion, in turn, modulates fracture aperture, thus achieving fluid–solid coupling in hydraulic fracturing. A schematic of the coupled model is presented in Figure 3. The governing equations for the coupled fluid–solid system are as follows:

$$\begin{cases} m_i \frac{d^2\mathbf{u}_i}{dt^2} = \sum_k \mathbf{F}_{i,k} + \sum_{j\in\Gamma_i}\left[-p(x,y,t)\mathbf{n}_j\Delta l_j\right] \\ I_i \frac{d^2\theta_i}{dt^2} = \sum_k M_{i,k} + \sum_{j\in\Gamma_i}\left[(\mathbf{r}_j - \mathbf{R}_i)\times\left(-p(x,y,t)\mathbf{n}_j\Delta l_j\right)\right] \\ \mathbf{q}(x,y,t) = -\frac{[f(\{\mathbf{u}_i(t),\theta_i(t)\})]^3}{12\mu}\nabla p(x,y,t) \\ \nabla\cdot\mathbf{q}(x,y,t) = 0 \end{cases} . \quad (1)$$

In Equation (1), m_i and I_i denote the mass and moment of inertia of a particle element, while $\mathbf{u}_i$ and θ_i represent its translational and rotational displacements. $\mathbf{F}_{i,k}$ and $M_{i,k}$ correspond to the resultant contact force and moment on the particle, respectively. Here, $\mathbf{r}_j$ is the centroid position vector of the particle boundary, $\mathbf{R}_i$ is the centroid position of the particle, $\mathbf{n}_j$ is the unit normal vector at the boundary, Γ_i denotes the set of all particle boundaries in contact with the fluid, and Δl_j is the length of the boundary segment. The fluid pressure and velocity fields are represented by p and $\mathbf{q}$, respectively. The fracture aperture, $w(x,y,t) = f(\{\mathbf{u}_i(t),\theta_i(t)\})$ depends on the particle displacements and satisfies the following condition for fracture nodes m and k:

$$w_{mk} = \begin{cases} \frac{w_0 F^n}{F_0 + F^n} & F^n < 0 \\ w_0 + \frac{(w_m + w_k)}{2} & F^n \geq 0 \end{cases} \quad (2)$$

In Equation (2), F_0 represents the normal force corresponding to a fracture aperture reduced to half of the initial aperture w_0; F^n denotes the normal stress at the boundary; and w_m, w_k is the boundary width at nodes m and k, expressed as a function of $\mathbf{u}_i(t)$ and $\theta_i(t)$. Assuming that particle elements i and j are adjacent to node m, the following relationship holds:

$$w_m = (\mathbf{u}_i - \mathbf{u}_j)\cdot\mathbf{n}_i + \theta_i\left[(\mathbf{r}_m - \mathbf{R}_i)^{\perp}\cdot\mathbf{n}_i\right] - \theta_j\left[(\mathbf{r}_m - \mathbf{R}_j)^{\perp}\cdot\mathbf{n}_i\right] \quad (3)$$

In essence, the boundary behavior is determined by the normal component of the relative motion between adjacent elements. In this context, $\mathbf{r}_m$ represents the coordinates of node m, $\mathbf{R}_i$ denotes the initial centroid position of particle element i, and $\mathbf{n}_i$ is the unit vector along the contact normal.

The governing equations are subject to the following boundary conditions:

(1) $\nabla\cdot\mathbf{q}(x,y,t) = Q_{in}$, representing constant-rate injection at the inlet;
(2) $\mathbf{u}_i(x=0, y=0) = 0$, with the left and bottom boundaries fixed;
(3) $\frac{\mathbf{F}_i(x=L)}{l_i} = \sigma_y$, $\frac{\mathbf{F}_i(y=L)}{l_i} = \sigma_x$, applying confining stresses at the model boundaries;
(4) The fracture tip pressure is assumed to be $p = P_a$, where P_a is an infinitesimally small value.

To ensure a controlled comparison, the coupled and uncoupled models used the same geometry, mineral distribution, Voronoi mesh, mechanical parameters, injection point, injection rate, in situ stress boundary conditions, and tensile/shear failure criteria. Thus, the only difference between the two models is the treatment of post-fracture hydro-mechanical feedback. The computational workflow of the present model is illustrated in Figure 4. Upon completion of fracture propagation calculations, fluid–solid coupling iterations are performed around the fracture network to dynamically update both fluid pressures and particle positions. In the uncoupled model, the effect of post-fracture fluid pressure changes on the solid is neglected, and fracture propagation is evaluated directly.

In contrast, the coupled model simulates the adjustment of fluid pressure and the evolution of fracture apertures through iterative fluid–solid interactions following fracture growth, as depicted in Figure 5. To enhance computational efficiency, the coupled model partitions the computational domain, focusing primarily on regions surrounding the fracture network, particularly at fracture tips, where fluid–solid interactions are most critical. The iteration process is controlled by a convergence criterion based on fluctuations in fracture apertures.

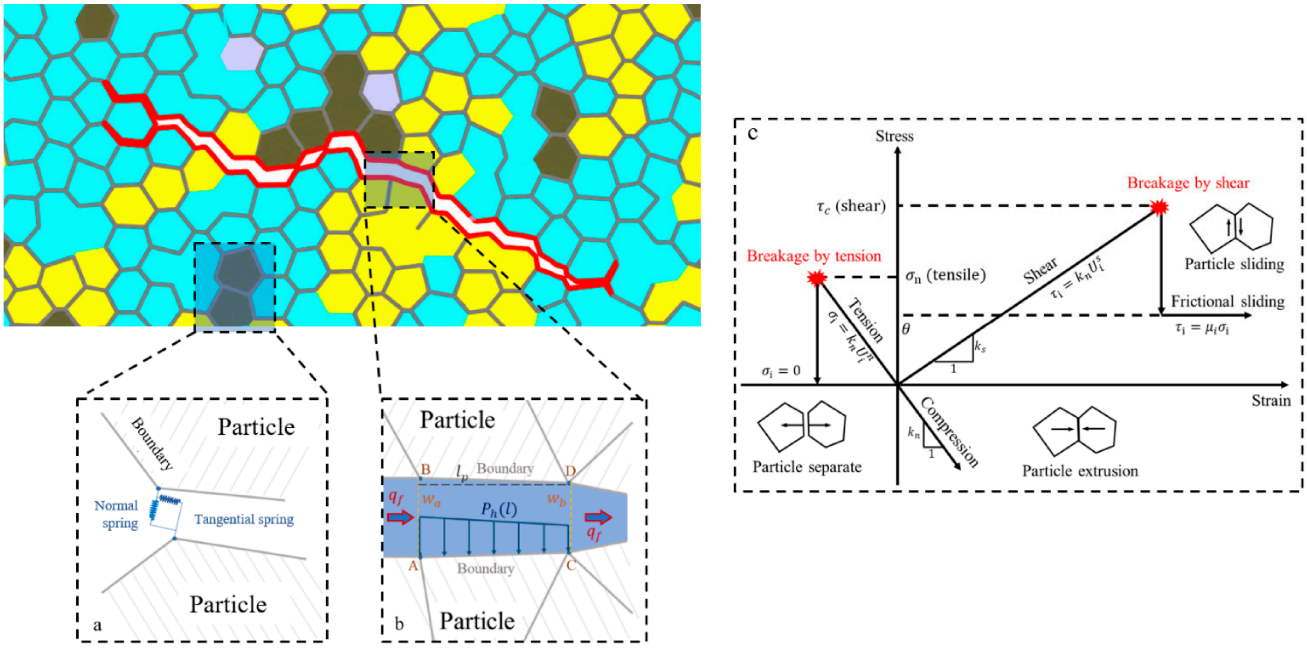


Figure 3. Schematic of the fluid–solid coupled model: (**a**) particle boundary spring configuration; (**b**) fluid elements; (**c**) stress–strain constitutive relationship of particle boundary springs.

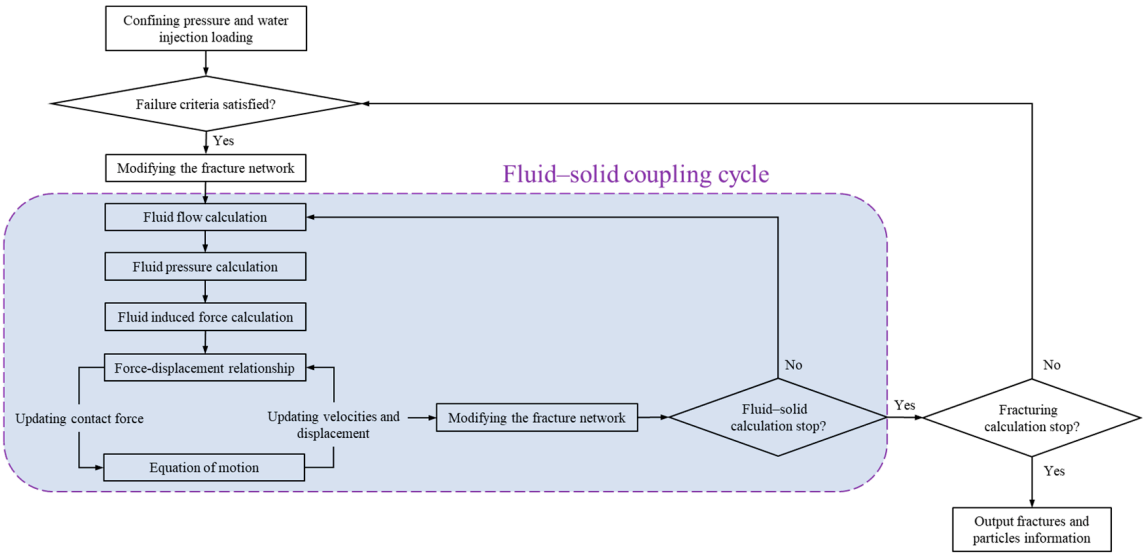


Figure 4. Iterative flowchart of the fluid–solid coupling procedure.

It should be noted that proppant transport was not explicitly simulated in this study. Instead, following the micro-proppant size range for tight sandstone reported in Reference [39], an equivalent minimum fracture aperture was imposed on the generated fractures. As fluid pressure dissipates during fracture propagation, the apertures near branch-fracture tips may decrease, but they are not allowed to fall below the prescribed minimum aperture. This treatment represents the residual hydraulic conductivity of propped or partially closed

fractures in an equivalent manner. The iteration and termination of the simulation are controlled by assessing fracture growth and setting appropriate fracture contact conditions. Upon completion, the model outputs detailed information on the fracture network, including fluid pressures and geometric parameters, and generates visualizations of the fracture network, particle displacements, and stress distributions.

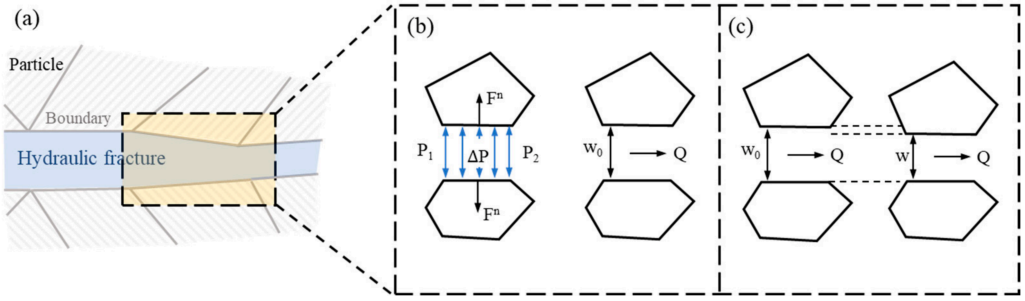
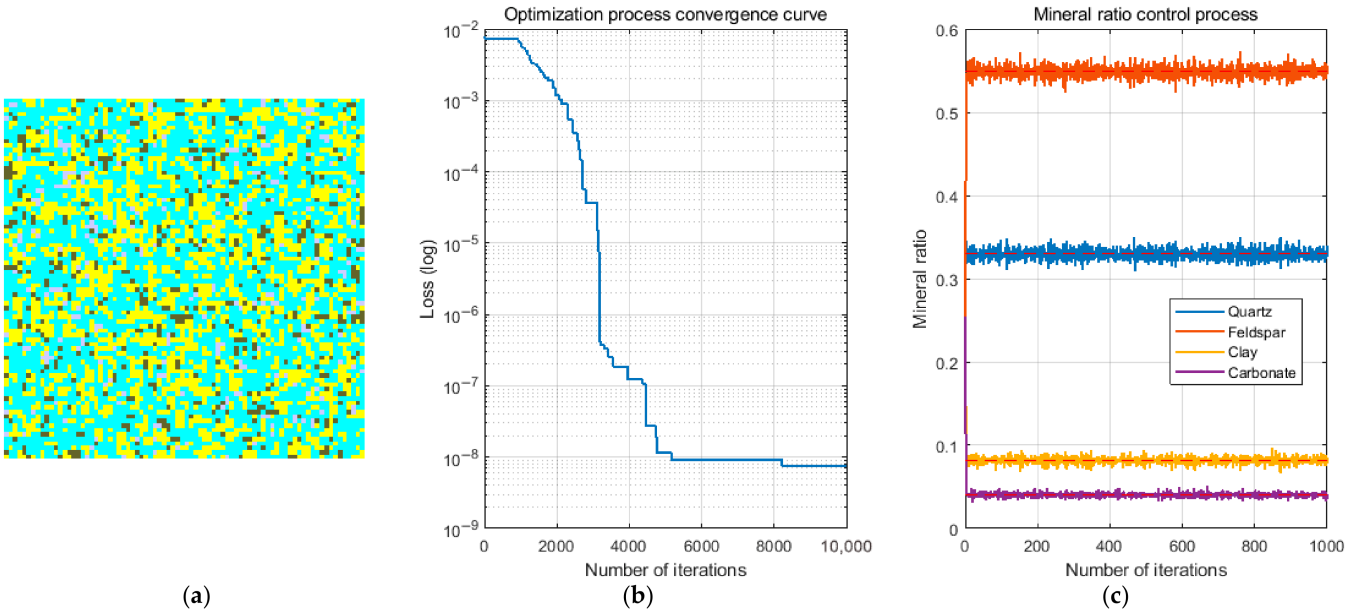


Figure 5. Schematic of the fluid–solid coupling: (**a**) fracture network; (**b**) initial fluid field and particle positions before coupling iteration; (**c**) fracture aperture evolution after coupling iteration.

3. Results and Discussion

3.1. Representative Analysis of the Random Mineral Distribution Model

As previously noted, the spatial distribution of minerals in rock has a significant impact on hydraulic fracturing outcomes. Consequently, the results of a multi-mineral rock model are considered generalizable only if the variance of simulation outcomes induced by random variations in micro-scale mineral distribution is statistically representative. To address this, Moran's I, a measure of spatial autocorrelation [40], was employed to quantify the spatial distribution patterns of minerals (clustered, dispersed, or random). For the four mineral components in the BSE-EDS image of tight sandstone shown in Figure 1, the Moran's I values are: quartz 0.184, feldspar 0.156, clay 0.108, and carbonate 0.124. Using a simulated annealing algorithm, mineral images were generated that satisfy both the target Moran's I values and the specified mineral proportions, as illustrated in Figure 6.



(**a**) (**b**) (**c**)

Figure 6. Simulated annealing algorithm for generating mineral distributions with target Moran's I and target proportions: (**a**) generated mineral image; (**b**) convergence curve of the loss function during optimization; (**c**) variation in the four mineral proportions during optimization.

To assess the variance in hydraulic fracturing outcomes arising from random micro-scale mineral distributions, five models were constructed with fixed mineral fractions (quartz 30%, feldspar 30%, clay 5%, carbonate 35%) and fixed Moran's I values (quartz 0.184, feldspar 0.156, clay 0.108, carbonate 0.124), but with randomized micro-scale arrangements. The results are model A–E, shown in Figure 7, indicating that random variations in mineral micro-distribution exert minimal influence on the primary fracture propagation, consistently producing three main fractures. Statistical analysis reveals that the coefficient of variation for fracture number per unit area is 9.7%, and for fracture length per unit area is 9.5%, a level considered statistically significant for tight rocks [41]. Accordingly, the multi-mineral hydraulic fracturing model of tight sandstone developed here can be regarded as broadly representative.

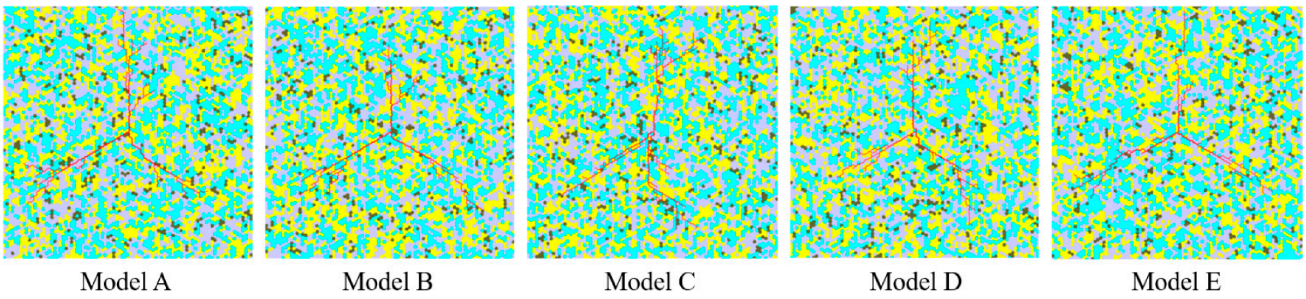


Figure 7. Comparison of model results with constant mineral proportions and Moran's I values, but random variations in micro-scale mineral distribution.

3.2. Model Comparison

3.2.1. Comparison Between Single-Mineral and Multi-Mineral Models

To assess the impact of fluid–solid coupling on hydraulic fracturing simulations, both the proposed coupled model and an uncoupled model were employed at an injection rate of 2 cm^2/min (differences in the uncoupled model are detailed in Section 2.2). An idealized single-mineral (quartz) model was constructed, with the resulting fracture networks illustrated in Figure 8. During the early stages of fracturing, both models produce identical propagation paths. However, as fracturing progresses, notable differences emerge: the coupled model generates a higher number of branch fractures, whereas the uncoupled model exhibits almost no branching. Statistical analysis shows that accounting for fluid–solid coupling increases the number of fractures by 41.8% and the total fracture length by 41.7%.

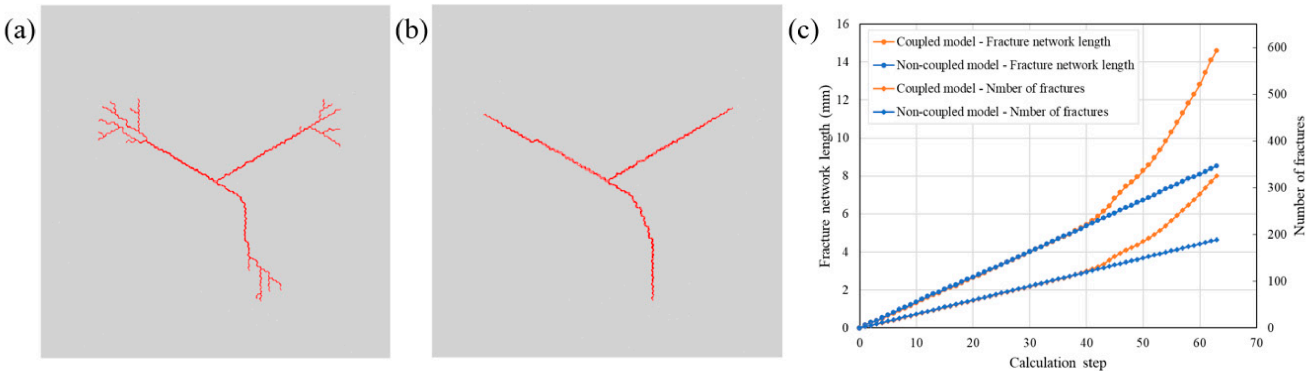


Figure 8. Fracture networks of the single-mineral hydraulic fracturing model: (**a**) coupled; (**b**) uncoupled; (**c**) statistical comparison.

For the multi-mineral tight sandstone hydraulic fracturing model developed in Section 3.1, the resulting fracture networks are illustrated in Figure 9. During the early stage of fracturing, both coupled and uncoupled models yield similar propagation paths.

However, as fracturing progresses, significant differences arise: the coupled model produces a higher number of branch fractures, whereas the uncoupled model generates fewer, predominantly at the distal ends of the fracture network. Statistical analysis shows that including fluid–solid coupling increases the number of fractures by 33.8% and the total fracture length by 34.1%. Overall, the uncoupled model substantially underestimates fracture propagation, particularly with respect to branch development in the later stages. Therefore, fluid–solid coupling must be accounted for in both highly heterogeneous rocks and relatively homogeneous single-mineral rocks.

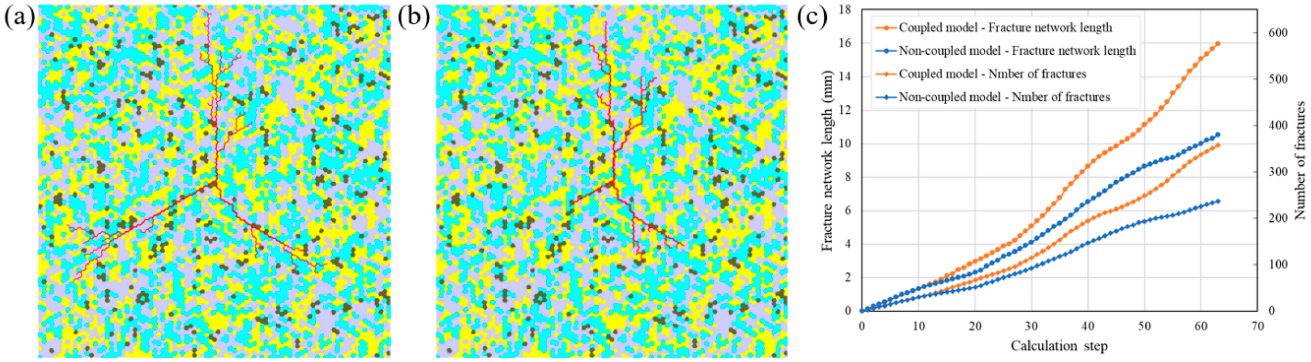


Figure 9. Fracture networks of the multi-mineral hydraulic fracturing model: (**a**) coupled; (**b**) uncoupled; (**c**) statistical comparison.

The mineral types on both sides of each effective fracture were statistically classified to evaluate the mineral dependence of fracture propagation, as shown in Table 3. In both the coupled and uncoupled models, fractures mainly occur along Feldspar–Feldspar and Quartz–Feldspar boundaries. These two boundary types account for 71.4% of the fractured boundaries in the coupled model and 63.7% in the uncoupled model. Quartz–Quartz and Feldspar–Calcite boundaries are also important fracture paths. Fractures involving calcite and clay minerals are present, but they mainly occur along mineral boundaries connected with these phases rather than through mineral interiors. Therefore, the observed propagation into calcite- or clay-rich regions should be interpreted as intergranular boundary failure. This result indicates that fracture propagation is mineral-boundary-dependent. The relatively weak bonding strength of mineral boundaries promotes fracture deflection, branching, and fracture network complexity, especially in the coupled model.

Table 3. Statistics of mineral types on both sides of fractures.

Fracture Mineral Types	Coupled Model	Uncoupled Model
Quartz–Quartz	11%	11.20%
Quartz–Feldspar	31.60%	30.50%
Quartz–Carbonate	4.70%	4.00%
Quartz–Clay	1.40%	4.50%
Feldspar–Feldspar	39.80%	33.20%
Feldspar–Carbonate	8.20%	9.00%
Feldspar–Clay	1.90%	5.40%
Calcite–Clay	1.40%	0.90%
Clay–Clay	0.00%	1.30%

3.2.2. Comparison with the Coupled Finite-Element Model

Using the commercial finite-element software ABAQUS (version CAE 2025) as a platform, the hydraulic fracturing process is simulated to compare the performance of the finite-element method and the discrete-element method in modeling hydraulic fracturing.

The fracture propagation results for the same single-mineral model are shown in Figure 10a. It can be seen that, due to the constraints imposed by the finite-element mesh, both the coupled single-mineral and multi-mineral finite-element models have difficulty reproducing multiple fractures along mineral grain boundaries and the evolution of complex branched fractures. Moreover, the number of mineral grains that can be included in the multi-mineral model is limited by the complexity of mesh generation; for example, the shale multi-mineral micro-model constructed in reference [42] contains only about 50 mineral grains. By contrast, the discrete-element model developed in this study can simulate complex hydraulic fracture networks and enables numerical analysis of multi-mineral grain models up to the representative elementary size (RES) (Supplementary Materials). For instance, the hydraulic fracturing model constructed herein comprises approximately 6900 grains.

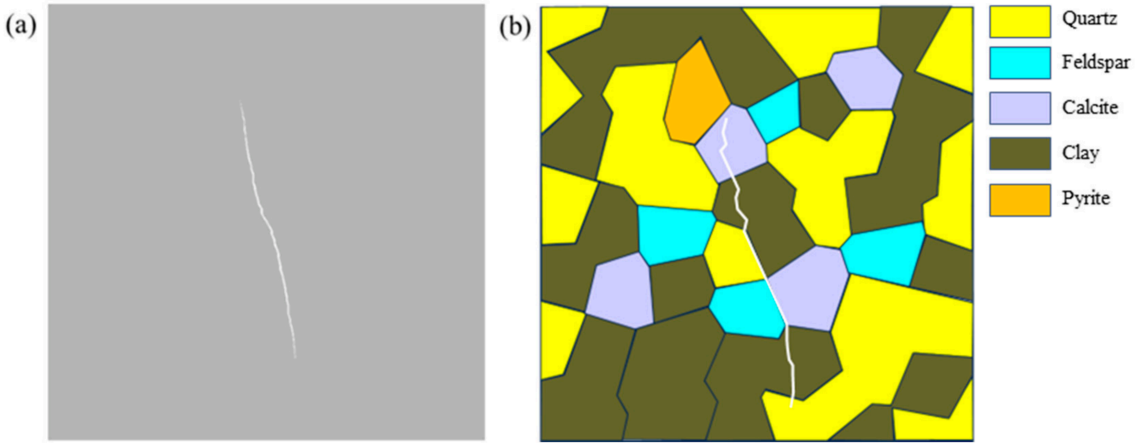


Figure 10. Fracture networks in finite-element hydraulic fracturing models: (**a**) single-mineral model; (**b**) multi-mineral model (modified from reference [42]).

3.3. Comparison of Breakdown Pressure

We designed coupled and uncoupled multi-mineral model cases under different injection-rate loadings to analyze how variations in fluid loading affect fracture initiation and propagation. We also note that the model injection rates are far lower than field conditions, necessitating an examination of field-to-model similarity criteria. Applying the Buckingham Π theorem to the hydraulic-fracturing process yields the key dimensionless groups that govern the process and are linked to injection rate:

$$\Pi_Q = \frac{Q\mu}{EL^3} \tag{4}$$

where Q denotes the injection rate, μ the fluid viscosity, E the Young's modulus of the rock, and L the characteristic length scale of hydraulic fracturing. This dimensionless group quantifies the contrast between the viscous effects required to keep fractures open and the rock's deformational stiffness.

After deriving the hydraulic-fracturing scaling laws, the field parameters (subscript f) are used to guide the design of the model parameters (subscript m):

$$Q_m = Q_f \left(\frac{L_m}{L_f}\right)^3 \frac{E_m}{E_f} \frac{\mu_f}{\mu_m} \tag{5}$$

Based on the hydraulic-fracturing design parameters for tight-sandstone reservoirs in the Linxing block on the northeastern margin of the Ordos Basin [43,44], namely an injection rate of 1–15 m^3 min^{-1}, a formation thickness of 5 m, and a fracturing-fluid viscosity of 250 mPa·s, substituting these values into Equation (4) yields a dimensionless group Π in

the range of (38–135) $\times 10^{-16}$. Using Equation (5), the corresponding model injection rate is obtained as 0.4–6.5 $cm^2\ min^{-1}$, from which the injection rate for the simulations in this study is selected.

According to classical hydraulic fracturing criteria, fracture initiation pressure is closely related to horizontal stress [45]; consequently, breakdown pressure is often used in hydraulic fracturing tests to estimate the maximum horizontal in situ stress. For example, reference [46] obtained breakdown pressure using a plane-strain numerical model and constructed a database from the simulation results to train an artificial neural network for predicting maximum horizontal stress, thereby providing insight into hydraulic fracturing performance. In hydraulic fracturing tests and this study, the breakdown pressure was defined as the maximum injection pressure reached immediately before the first rapid pressure drop and unstable fracture propagation.

Breakdown pressures under various injection rates for both coupled and uncoupled models are presented in Figure 11. Regardless of coupling, the effect of injection rate on breakdown pressure follows the same trend: breakdown pressure increases with increasing injection rate. However, in the coupled model, rock deformation feedback plays a key role; fluid injection compresses the rock, placing the fracture tip under high compressive stress and enhancing local closure stress. Consequently, a higher fluid pressure accumulation is required to initiate fracturing, resulting in greater breakdown pressures in the coupled model.

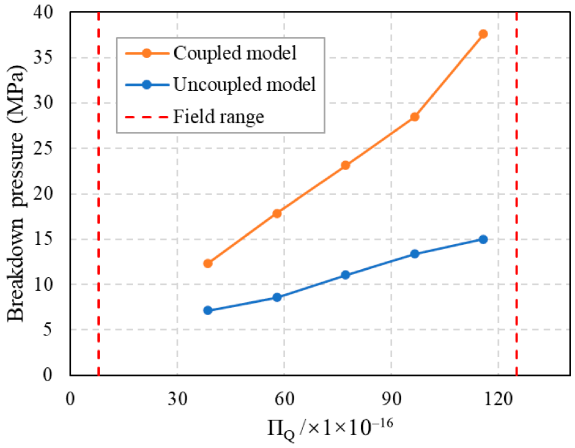


Figure 11. Variation in breakdown pressure with injection rate.

3.4. Comparison of Fracture Network Propagation Characteristics

As shown in Figure 12a, the number of fractures per unit area varies with injection rate. For Model A (the multi-mineral tight-sandstone model constructed in Section 3.1), the coupled simulations exhibit a non-monotonic trend: the fracture density first increases and then decreases as the injection rate rises. To interrogate this behavior, we held the mineral proportions and Moran's I constant, thereby keeping the model's dimensionless group Π unchanged under identical parameters, and computed the fracture network counts for Models B-E obtained by randomizing the mineral distribution in Figure 7. The resulting trends in Figure 12a differ among models: for Models A and E, fracture counts increase and then decrease; for Models B and D, they increase monotonically; for Model C, they increase, then decrease, and increase again. These patterns indicate that the dependence of fracture network abundance on injection rate is controlled by the mineral distribution, consistent with Zheng (2023) [8], who reports that the injection-rate dependence of fracture counts is governed by rock properties. In Figure 12b, the difference between coupled and uncoupled simulations is defined as $\Delta = (N_{coupled} - N_{uncoupled})/N_{coupled} \times 100\%$. Across the models with randomized mineral distributions, $\Delta > 0$ for all injection rates, indicating

that the coupled simulations yield more fractures than the uncoupled ones. The average difference is 28.7%, with a maximum of 67.2%.

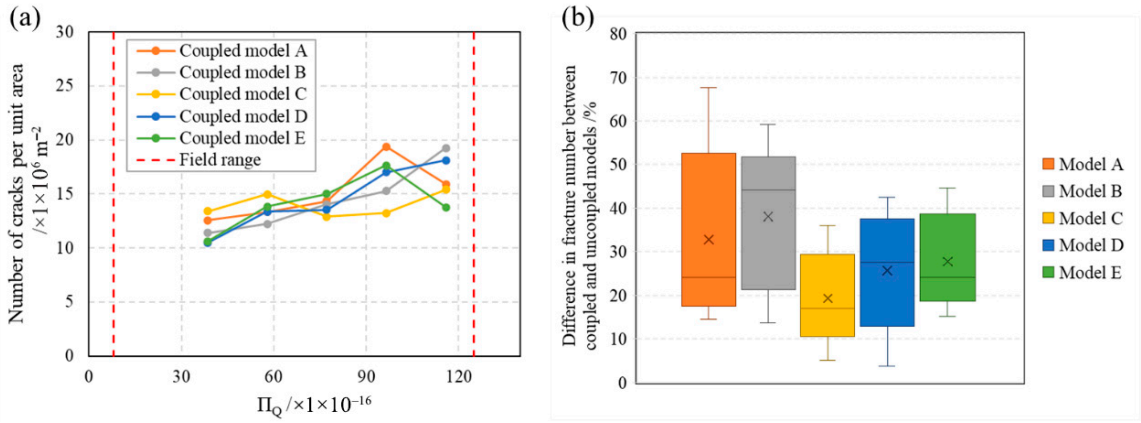


Figure 12. (**a**) Number of fractures per unit area under different injection rates; (**b**) Difference in fracture counts between coupled and uncoupled simulations.

To clarify why the coupled simulations produce more fractures than the uncoupled ones, we tracked fracture-tip fluid pressure throughout network growth and analyzed it alongside mapped propagation fronts (Figure 13). Five representative steps (1–5) were selected, and concentric envelopes of fracture extent were constructed to compare propagation in the two formulations. Stage I. Near the injection point, the main fracture initiates and extends; coupled and uncoupled responses are similar, with comparable trajectories and reach. Stage II. With continued injection, the coupled model exhibits the nucleation and growth of branch fractures, whereas the left-side fracture in the uncoupled model arrests owing to insufficient tip pressure, revealing emerging morphological differences. Stage III. Multilevel branching in the coupled case advances further, producing a more intricate network; in the uncoupled case, only the upper fracture continues to grow, while the left and right fractures stall due to pressure deficits. The disparity in network development therefore widens. Quantitatively, during Stages I–III the coupled tip pressure is approximately six times that of the uncoupled case. Stage IV. The coupled tip pressure becomes markedly higher, up to approximately 40 times, because propagation in the uncoupled model has nearly ceased, leaving a tip pressure of only 0.02 MPa, whereas the coupled model continues to accumulate tip pressure and drive further advance. These observations are corroborated by the magnified segments of the tip-pressure curves and the zoomed region in the lower-right of the propagation map. Taken together, the coupled model reproduces the mechanism of pressure-buildup-driven tip advance, while the uncoupled model prematurely halts fracture growth and substantially underestimates network initiation and propagation. At calculation step = 100, fractures intersect the model boundaries and the simulation is terminated by the domain size; continued integration would likely further amplify the divergence between the two cases.

With increasing injection rate, fracture-tip pressure rises and the uncoupled formulation can also sustain propagation of the left and right primary fractures (Figure 14). At these rates, the mean tip pressure in the coupled model is approximately threefold that of the uncoupled model, less than the approximately six times the ratio at low rates (Figure 13), and the extreme, order-of-magnitude disparity associated with arrested growth in the uncoupled case no longer occurs. Despite this convergence in tip pressure, the coupled simulations still yield a larger number of fractures. The difference is rooted in the propagation chronology: (i) Early stage. Onset and early growth of the main fracture are broadly similar in both models. (ii) Intermediate stage. The increased driving force

at higher rates enables the uncoupled model to rapidly generate first-order, quasi-linear branches. (iii) Late stage. The coupled model continues to evolve into a multilayered, more intricate network with additional branching, whereas the uncoupled model primarily extends the first-order linear branches together with the main fracture. Moreover, the rapid advance of the main fracture in the uncoupled case drives the network front to the model boundary earlier, prematurely halting growth. By contrast, the coupled model reaches the boundary at a later step, allowing more extensive branching to develop.

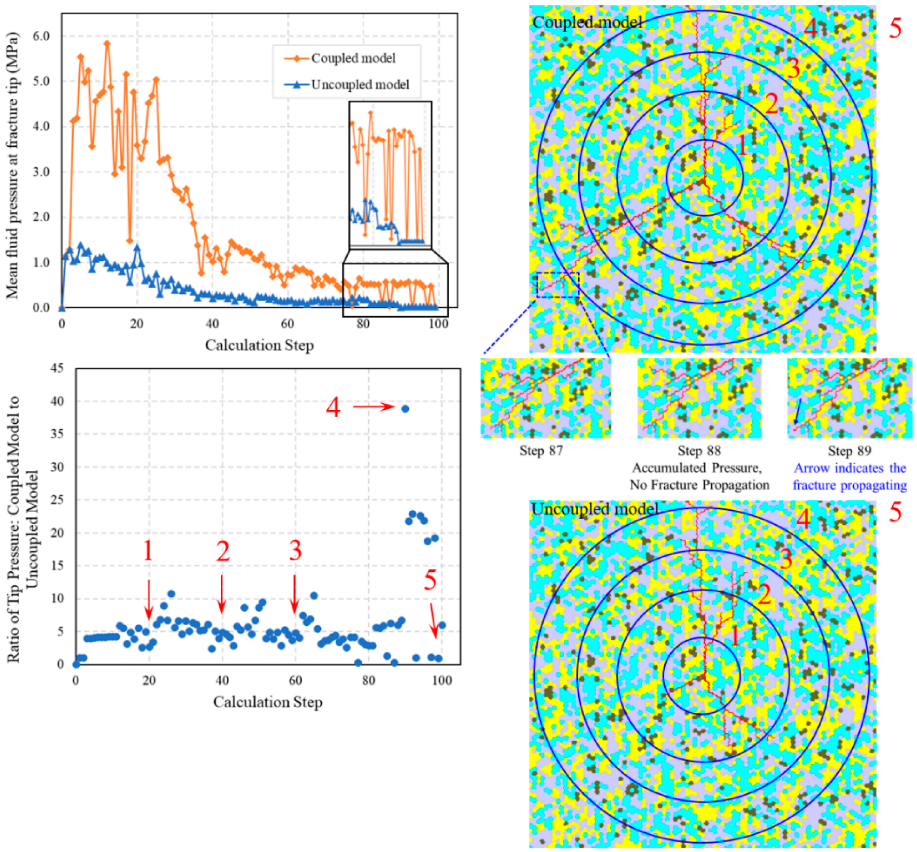


Figure 13. $\Pi_Q = 38.6 \times 10^{-16}$ (Q = 2cm^2/min) case: Fracture-tip fluid-pressure evolution curves and fracture network propagation maps for the coupled and uncoupled models. Labels 1–5 correspond to concentric envelopes of fracture extent 1–5.

Figures 13 and 14 show that, during network growth, the coupled model experiences a substantially larger fracture-tip pressure drop, whereas the uncoupled model incurs only minor losses and sustains an almost constant tip pressure. Two mechanisms underpin this divergence. (i) The uncoupled formulation is governed primarily by the advance of the main fracture with limited branching, while the coupled formulation develops extensive, multilevel branching. The pressure required to open branch fractures and reorient propagation paths is dissipated, producing a pronounced decline in tip pressure as the network enlarges. (ii) The coupled simulations resolve pressure losses arising from fluid–solid coupling, particularly acute at fracture tips, whereas the uncoupled simulations omit these coupling-induced drops. Within the fracture, the relationship between flow rate and fluid pressure gradient obeys the cubic law: $q = -\frac{w^3}{12\mu}\frac{dp_f}{ds}$, where q is the unit-height flow rate, w is the fracture aperture, μ is the fluid viscosity, p_f is the fluid pressure within the fracture, and s is the arc-length coordinate along the fracture. Therefore, it follows that

$$\frac{dp_f}{ds} = -\frac{12\mu q}{w^3} \tag{6}$$

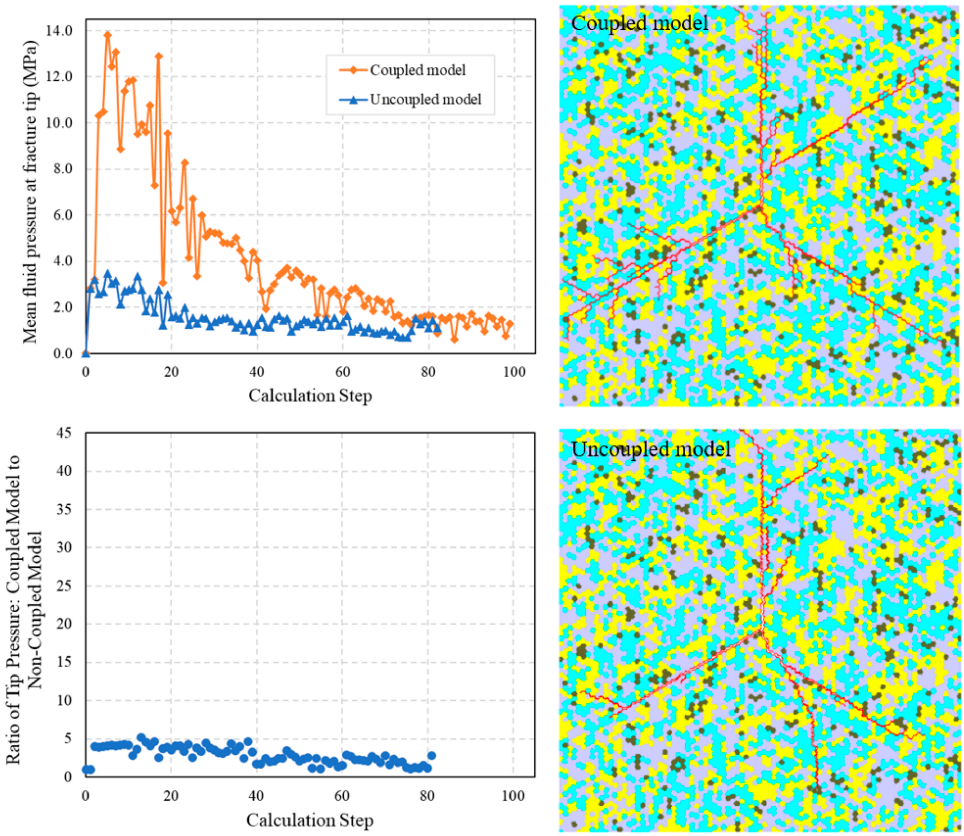


Figure 14. $\Pi_Q = 96.5 \times 10^{-16}$(Q = 5 cm^2/min) case: fracture-tip fluid-pressure evolution curves and fracture network propagation maps for the coupled and uncoupled models.

The fracture aperture is determined by the difference between the fluid pressure and the normal stress of the rock: $p_{net}(s) = p_f - \sigma_n(s)$, where $\sigma_n(s)$ is the normal closure stress on the fracture surface. Therefore, we have

$$\frac{dp_f}{ds} = \frac{dp_{net}}{ds} + \frac{d\sigma_n}{ds} \tag{7}$$

By combining Equations (6) and (7), we obtain

$$\frac{dp_{net}}{ds} = -\frac{12\mu q}{w^3} - \frac{d\sigma_n}{ds} \tag{8}$$

According to Equation (8), the net pressure drop across any segment of the fracture can be decomposed into two components:

$$\Delta p_{net} = \Delta p_{visc} + \Delta p_{cpl} \tag{9}$$

where

$$\begin{aligned} \Delta p_{visc} &= \int_{s_1}^{s_2} \left(\frac{12\mu q}{w^3}\right) ds \\ \Delta p_{cpl} &= \int_{s_1}^{s_2} \left(\frac{d\sigma_n}{ds}\right) ds = \sigma_n(s_2) - \sigma_n(s_1) \end{aligned} \tag{10}$$

where Δp_{visc} represents the viscous pressure drop, governed by the cubic law and dependent on flow rate, fracture aperture, and fluid viscosity. It varies smoothly and continuously along the fracture and is present in both the coupled and uncoupled models. Δp_{cpl} denotes the pressure drop due to coupling effects, determined by the spatial variation in the solid's normal stress distribution; it is significant in the coupled model but absent in the uncoupled model. According to classical linear elastic fracture mechanics, the leading-order

near-tip stress field exhibits an inverse-square-root singularity, i.e., $\sigma \sim 1/\sqrt{r}$, where r is the distance from the fracture tip. Although the discrete-element model does not produce a mathematical singularity because of its finite particle scale, it captures a pronounced near-tip stress concentration and a corresponding variation in the normal closure stress. Therefore, compared with the uncoupled model, the coupled model exhibits a larger tip fluid pressure drop.

In summary, the uncoupled model admits no feedback from solid deformation during fracture growth. Once failure initiates, the injection pressure remains essentially constant, preventing further pressure build-up; propagation is thus confined to the primary fracture and fails to generate complex, multi-order branching. By contrast, in the coupled model fluid energy is more effectively dissipated in physically relevant processes, such as opening branches, redirecting the propagation path, and overcoming stress-shadow interactions among branches, leading to a pronounced crack-tip pressure drop. Consequently, the coupled model sustains and evolves a more complex fracture network that better reflects the underlying physics.

4. Conclusions

Based on the spatial distribution and equivalent mechanical properties of the main mineral groups in tight sandstone, this study constructs a hydraulic-fracturing model using a two-dimensional polygonal discrete-element method and explicitly couples fluid elements with intergranular particles to simulate fracture growth. The multi-mineral tight-sandstone model is sized to a representative elementary area for mineral distributions, ensuring that the results are not biased by stochastic microscale heterogeneity. We systematically compare the coupled and uncoupled formulations and investigate how variations in fluid loading govern the initiation and propagation of fracture networks in tight sandstone:

(1) Fluid–solid coupling exerts a primary control on network complexity. Over the range of injection rates considered, the coupled simulations consistently yield higher fracture counts than the uncoupled simulations, with a mean excess of 28.7% and a maximum of 67.2%.

(2) Breakdown pressure is significantly higher in the coupled model than in the uncoupled counterpart and exhibits a positive correlation with injection rate.

(3) The coupled model predicts substantially higher fracture-tip pressures than the uncoupled model and exhibits pronounced tip-pressure declines during initiation and propagation. These declines indicate enhanced dissipation of fluid energy into branch opening and trajectory reorientation, thereby sustaining the evolution of more complex and physically realistic networks. Accordingly, at low injection rates the coupled formulation captures pressure-buildup-driven tip advance, whereas the uncoupled formulation fails to maintain propagation; at higher rates the coupled formulation develops multilayered, highly branched networks, while the uncoupled formulation produces only simple, first-order branching.

It should be noted that the present model is formulated at the mineral-particle scale and is intended to elucidate the mechanisms of fracture initiation and growth at small scales. Extending hydraulic fracturing simulations to larger scales is a prospective direction for future research.

Supplementary Materials: The following supporting information can be downloaded at https://www.mdpi.com/article/10.3390/min16050540/s1, Figure S1: "penny" model forms fractures with single-directional expansion under the influence of injected fluid and confining pressure [47]; Figure S2: Equivalent model for calculating the growth of a single fracture [48]; Figure S3: Relationship between the distance from fracture center and the aperture of fracture; Figure S4: HSW-1000B

microcomputer-controlled electro-hydraulic servo rock triaxial instrument (a) and rock fixture for Brazilian splitting experiment (b); Figure S5: Comparison of stress–strain curves for tight sandstone cores and models under Brazilian splitting tests; Table S1: Calculation of injection parameters for single fracture growth by equivalent model and "penny" model.

Author Contributions: M.L. and X.Q. conceptualized and designed the study. X.Q. developed the methodology and conducted the formal analysis. W.D. conducted the investigation, curated data, and performed visualization. X.Q. wrote the original draft. M.L. reviewed and edited the manuscript. W.J., G.C. and L.J. acquired funding, administered the project, and provided resources. All authors have read and agreed to the published version of the manuscript.

Funding: This work was supported by the National Natural Science Foundation of China (Grant No. 42030808), the Project of Chinese Academy of Sciences (CAS04010303), and the Strategic Priority Research Program of the Chinese Academy of Sciences (Grant No. XDA14010304 and No. XDA0430103).

Data Availability Statement: The datasets used and/or analyzed during the current study are available from the corresponding author on reasonable request.

Conflicts of Interest: The authors do not have any competing or conflicting interest to declare.

References

1. Hu, S.; Wu, Y.; Yan, Y.; Huo, T.; Xu, Z.; Li, Y.; He, J.; Zhang, W.; Wang, D. Parameter optimization study of three-dimensional well network-fracture network coupled fracturing in Jimsar shale oil. *Unconv. Resour.* **2024**, *4*, 100102. [CrossRef]
2. Gong, X.; Ma, X.; Liu, Y. Analysis of geological factors affecting propagation behavior of fracture during hydraulic fracturing shale formation. *Geomech. Geophys. Geo-Energy Geo-Resour.* **2024**, *10*, 102. [CrossRef]
3. Li, J.; Dong, S.; Hua, W.; Li, X.; Pan, X. Numerical investigation of hydraulic fracture propagation based on cohesive zone model in naturally fractured formations. *Processes* **2019**, *7*, 28. [CrossRef]
4. Li, Y.Y.; Hu, W.; Zhang, Z.H.; Zhang, Z.B.; Shang, Y.J.; Han, L.L.; Wei, S.Y. Numerical simulation of hydraulic fracturing process in a naturally fractured reservoir based on a discrete fracture network model. *J. Struct. Geol.* **2021**, *147*, 104331. [CrossRef]
5. Chen, B.; Ramos Barboza, B.; Sun, Y.; Bai, J.; Thomas, H.R.; Dutko, M.; Cottrell, M.; Li, C. A review of hydraulic fracturing simulation. *Arch. Comput. Methods Eng.* **2022**, *29*, 1–58. [CrossRef]
6. Li, Z.; Li, L.; Huang, B.; Zhang, L.; Li, M.; Zuo, J.; Li, A.; Yu, Q. Numerical investigation on the propagation behavior of hydraulic fractures in shale reservoir based on the DIP technique. *J. Pet. Sci. Eng.* **2017**, *154*, 302–314. [CrossRef]
7. Huang, L.; He, R.; Yang, Z.; Tan, P.; Chen, W.; Li, X.; Cao, A. Exploring hydraulic fracture behavior in glutenite formation with strong heterogeneity and variable lithology based on DEM simulation. *Eng. Fract. Mech.* **2023**, *278*, 109020. [CrossRef]
8. Zheng, S.P. Study of the Growth Mechanism of Microfracture Networks in Tight Sandstones. Ph.D. Thesis, University of Chinese Academy of Sciences, Beijing, China, 2023.
9. Dou, F.; Wang, J.G. A numerical investigation for the impacts of shale matrix heterogeneity on hydraulic fracturing with a two-dimensional particle assemblage simulation model. *J. Nat. Gas Sci. Eng.* **2022**, *104*, 104678. [CrossRef]
10. Kong, L.; Ranjith, P.G.; Li, B.Q. Fluid-driven micro-cracking behaviour of crystalline rock using a coupled hydro-grain-based discrete element method. *Int. J. Rock Mech. Min. Sci.* **2021**, *144*, 104766. [CrossRef]
11. Kong, L.; Ranjith, P.G.; Li, Q.B.; Song, Y. Rock grain-scale mechanical properties influencing hydraulic fracturing using Hydro-GBM approach. *Eng. Fract. Mech.* **2022**, *262*, 108227. [CrossRef]
12. Li, M.; Wu, J.; Li, J.; Zhuang, L.; Wang, S.; Zhang, F. Modeling of hydraulic fracturing in polymineralic rock with a grain-based DEM coupled with a pore network model. *Eng. Fract. Mech.* **2022**, *275*, 108801. [CrossRef]
13. Wang, S.; Zhou, J.; Zhang, L.; Han, Z.; Kong, Y. Numerical insight into hydraulic fracture propagation in hot dry rock with complex natural fracture networks via fluid-solid coupling grain-based modeling. *Energy* **2024**, *295*, 131060. [CrossRef]
14. Pei, Y.; Zhang, N.; Zhou, H.; Zhang, S.; Zhang, W.; Zhang, J. Simulation of multiphase flow pattern, effective distance and filling ratio in hydraulic fracture. *J. Pet. Explor. Prod. Technol.* **2020**, *10*, 585–597. [CrossRef]
15. Gu, H.; Siebrits, E. Effect of formation modulus contrast on hydraulic fracture height containment. *SPE Prod. Oper.* **2008**, *23*, 170–176. [CrossRef]
16. Adachi, J.-I.; Detournay, E.; Peirce, A.P. Analysis of the classical pseudo-3D model for hydraulic fracture with equilibrium height growth across stress barriers. *Int. J. Rock Mech. Min. Sci.* **2010**, *47*, 625–639. [CrossRef]
17. Perkins, T.K.; Kern, L.R. Widths of hydraulic fractures. *J. Pet. Technol.* **1961**, *13*, 937–949. [CrossRef]
18. Nordgren, R.P. Propagation of a vertical hydraulic fracture. *Soc. Pet. Eng. J.* **1972**, *12*, 306–314. [CrossRef]
19. Secchi, S.; Schrefler, B.A. A method for 3-D hydraulic fracturing simulation. *Int. J. Fract.* **2012**, *178*, 245–258. [CrossRef]

20. Fu, P.; Johnson, S.M.; Carrigan, C.R. An explicitly coupled hydro-geomechanical model for simulating hydraulic fracturing in arbitrary discrete fracture networks. *Int. J. Numer. Anal. Methods Geomech.* **2013**, *37*, 2278–2300. [CrossRef]
21. Haddad, M.; Sepehrnoori, K. Simulation of multiple-stage fracturing in quasibrittle shale formations using pore pressure cohesive zone model. In Proceedings of the 2nd Unconventional Resources Technology Conference (URTeC), Denver, CO, USA, 25–27 August 2014. [CrossRef]
22. Gao, Q.; Cheng, Y.; Yan, C. A 3D numerical model for investigation of hydraulic fracture configuration in multilayered tight sandstone gas reservoirs. *J. Pet. Explor. Prod. Technol.* **2018**, *8*, 1413–1424. [CrossRef]
23. Zhu, W.; He, X.; Chen, Z.; Tian, Z.; Wang, M. Numerical investigation of influential factors in hydraulic fracturing processes using coupled discrete element-lattice Boltzmann method. *J. Geophys. Res. Solid Earth* **2023**, *128*, e2023JB027292. [CrossRef]
24. Chen, Z.; Wang, M. Pore-scale modeling of hydromechanical coupled mechanics in hydrofracturing process. *J. Geophys. Res. Solid Earth* **2017**, *122*, 3410–3429. [CrossRef]
25. Yang, W.; Lv, X.; Wang, L.; Peng, D.; Chen, X. A DEM-CFD coupling method for modelling two-hole synchronous hydraulic fracturing. *Geomech. Geophys. Geo-Energy Geo-Resour.* **2023**, *9*, 6. [CrossRef]
26. Ni, X.D.; Zhu, C.; Wang, Y. Hydro-mechanical analysis of hydraulic fracturing based on an improved DEM-CFD coupling model at micro-level. *J. Comput. Theor. Nanosci.* **2015**, *12*, 2691–2700. [CrossRef]
27. Wang, Y.; Wang, S.; Xue, S.; Adhikary, D. Numerical modeling of porous flow in fractured rock and its applications in geothermal energy extraction. *J. Earth Sci.* **2015**, *26*, 20–27. [CrossRef]
28. Yao, Y.; Guo, Z.; Zeng, J.; Li, D.; Lu, J.; Liang, D.; Jiang, M. Discrete element analysis of hydraulic fracturing of methane hydrate-bearing sediments. *Energy Fuels* **2021**, *35*, 6644–6657. [CrossRef]
29. Zhang, J.; Yu, H.; Wang, Q.; Lv, C.; Liu, C.; Shi, F.; Wu, H. Hydraulic fracture propagation at weak interfaces between contrasting layers in shale using XFEM with energy-based criterion. *J. Nat. Gas Sci. Eng.* **2022**, *101*, 104502. [CrossRef]
30. Luo, Z.; Cheng, L.; Zhao, L.; Xie, Y. Numerical simulation and analysis of thermo-hydro-mechanical behaviors of hydraulic fracturing in naturally fractured formation using a THM-XFEM coupling model. *J. Nat. Gas Sci. Eng.* **2022**, *103*, 104657. [CrossRef]
31. Ni, L.; Zhang, X.; Zou, L.; Huang, J. Phase-field modeling of hydraulic fracture network propagation in poroelastic rocks. *Comput. Geosci.* **2020**, *24*, 1767–1782. [CrossRef]
32. Zhuang, X.; Li, X.; Zhou, S. Transverse penny-shaped hydraulic fracture propagation in naturally-layered rocks under stress boundaries: A 3D phase field modeling. *Comput. Geotech.* **2023**, *155*, 105205. [CrossRef]
33. Sarmadi, N.; Mousavi Nezhad, M. Phase-field modelling of fluid driven fracture propagation in poroelastic materials considering the impact of inertial flow within the fractures. *Int. J. Rock Mech. Min. Sci.* **2023**, *169*, 105444. [CrossRef]
34. Sharafisafa, M.; Sato, A.; Aliabadian, Z. Hydraulic fracture development in conglomerate reservoirs simulated using combined finite-discrete element method. *Eng. Fract. Mech.* **2023**, *279*, 109063. [CrossRef]
35. Dou, W.; Lin, M.; Jiang, W.; Ji, L.; Cao, G. Importance of diagenetic heterogeneity in Chang 7 sandstones for modeling CO_2-water-rock interactions. *Int. J. Greenh. Gas Control* **2024**, *132*, 104018. [CrossRef]
36. Li, W.H.; Lu, S.F.; Wang, M.; Zhou, N.; Cheng, Z. Quantitative characterization of micro heterogeneity of tight reservoirs by large-view FE-SEM splicing technology. *Oil Gas Geol.* **2022**, *43*, 1497–1504.
37. Liu, S.J. The Micro Heterogeneity Controlling Mechanism of Tensile Fracture in Crystalline Rocks. Ph.D. Thesis, Chang'an University, Xi'an, China, 2023.
38. Wang, S.; Zhou, J.; Zhang, L.; Han, Z.; Zhang, F. Parameter studies on the mineral boundary strength influencing the fracturing of the crystalline rock based on a novel grain-based model. *Eng. Fract. Mech.* **2021**, *241*, 107388. [CrossRef]
39. Li, B.; Li, Y.; Zhou, F.; Tian, Y.; Yuan, S.; Li, H. Production enhancement mechanism of micro-proppant and its selection principles for shale oil and gas. *Geol. Explor.* **2020**, *56*, 627–634.
40. Moran, P.A.P. Notes on continuous stochastic phenomena. *Biometrika* **1950**, *37*, 17–23. [CrossRef]
41. Wang, Z.; Wang, T.; Wang, W.; Zhang, Z. Size of representative elementary volume for heterogeneous rocks evaluated using distinct element method. *Acta Geotech.* **2023**, *18*, 1883–1900. [CrossRef]
42. Hou, M.; Liang, B.; Sun, W.; Liu, Q. Influence of mineral interface stiffness on fracture propagation law of shale hydraulic fracturing. *Pet. Reserv. Eval. Dev.* **2023**, *13*, 100–107.
43. Fang, M.; Du, X.; Bai, Y.; Li, H.; Zhang, H.; Zhu, H. Three-dimensional physical simulation experiments on large-scale hydraulic fracturing in multi-thin interbedded tight sandstone reservoirs. *Exp. Pet. Geol.* **2024**, *46*, 786–798.
44. Yang, F.; Mei, W.; Li, L.; Sun, Z.; An, Q.; Yang, Q.; Lu, M.; Yang, R. Propagation of hydraulic fractures in thin interbedded tight sandstones. *Coal Geol. Explor.* **2023**, *51*, 61–71.
45. Hubbert, M.K.; Willis, D.G. Mechanics of hydraulic fracturing. *Pet. Trans. AIME* **1957**, *210*, 153–168. [CrossRef]
46. Lakirouhani, A.; Jolfaei, S. Hydraulic fracturing breakdown pressure and prediction of maximum horizontal in situ stress. *Adv. Civ. Eng.* **2023**, *2023*, 8180702. [CrossRef]

47. Abdollahipour, A.; Fatehi Marji, M.; Yarahmadi Bafghi, A.; Gholamnejad, J. DEM simulation of confining pressure effects on crack opening displacement in hydraulic fracturing. *Int. J. Min. Sci. Technol.* **2016**, *26*, 557–561. [CrossRef]
48. Paulick, M.; Morgeneyer, M.; Kwade, A. Review on the influence of elastic particle properties on DEM simulation results. *Powder Technol.* **2015**, *283*, 66–76. [CrossRef]

Disclaimer/Publisher's Note: The statements, opinions and data contained in all publications are solely those of the individual author(s) and contributor(s) and not of MDPI and/or the editor(s). MDPI and/or the editor(s) disclaim responsibility for any injury to people or property resulting from any ideas, methods, instructions or products referred to in the content.